This article was downloaded by: *[Webb, B. W.]*
On: *5 October 2010*
Access details: *Access Details: [subscription number 927412860]*
Publisher *Taylor & Francis*
Informa Ltd Registered in England and Wales Registered Number: 1072954 Registered office: Mortimer House, 37-41 Mortimer Street, London W1T 3JH, UK

Combustion Science and Technology
Publication details, including instructions for authors and subscription information:
http://www.informaworld.com/smpp/title~content=t713456315

Time-Resolved Radiation and Convection Heat Transfer in Combusting Discontinuous Fuel Beds

David Frankman[a]; Brent W. Webb[a]; Bret W. Butler[b]
[a] Department of Mechanical Engineering, Brigham Young University, Provo, UT, USA [b] U.S. Forest Service, Rocky Mountain Research Station, Fire Sciences Laboratory, Missoula, MT, USA

Online publication date: 29 September 2010

To cite this Article Frankman, David , Webb, Brent W. and Butler, Bret W.(2010) 'Time-Resolved Radiation and Convection Heat Transfer in Combusting Discontinuous Fuel Beds', Combustion Science and Technology, 182: 10, 1391 — 1412
To link to this Article: DOI: 10.1080/00102202.2010.486388
URL: http://dx.doi.org/10.1080/00102202.2010.486388

PLEASE SCROLL DOWN FOR ARTICLE

Full terms and conditions of use: http://www.informaworld.com/terms-and-conditions-of-access.pdf

This article may be used for research, teaching and private study purposes. Any substantial or systematic reproduction, re-distribution, re-selling, loan or sub-licensing, systematic supply or distribution in any form to anyone is expressly forbidden.

The publisher does not give any warranty express or implied or make any representation that the contents will be complete or accurate or up to date. The accuracy of any instructions, formulae and drug doses should be independently verified with primary sources. The publisher shall not be liable for any loss, actions, claims, proceedings, demand or costs or damages whatsoever or howsoever caused arising directly or indirectly in connection with or arising out of the use of this material.

Combust. Sci. and Tech., 182: 1391–1412, 2010
Copyright © Taylor & Francis Group, LLC
ISSN: 0010-2202 print/1563-521X online
DOI: 10.1080/00102202.2010.486388

Downloaded By: [Webb, B. W.] At: 18:23 5 October 2010

TIME-RESOLVED RADIATION AND CONVECTION HEAT TRANSFER IN COMBUSTING DISCONTINUOUS FUEL BEDS

David Frankman,[1] Brent W. Webb,[1] and Bret W. Butler[2]
[1]*Department of Mechanical Engineering, Brigham Young University, Provo, UT, USA*
[2]*U.S. Forest Service, Rocky Mountain Research Station, Fire Sciences Laboratory, Missoula, MT, USA*

Time-resolved radiation and convection heat flux were measured in a series of experimental fires designed to explore heat transfer behavior during the combustion of discontinuous fuel beds. Fuel spacing and height were varied for both buoyancy- and wind-driven combustion. Peak radiation and convection heat fluxes as high as 130 kW/m^2 were recorded. Radiation flux had the effect of heating the fuel before flame arrival. Both positive (heating) and negative (cooling) convective heat transfer occurred before flame arrival. Surprisingly, the convection could also be positive or negative after flame arrival, indicating that even when engulfed in flames there were packets of cooler air moving across the sensor. In nearly all cases, short-duration convective heating pulses appear to precede the full onset of combustion, suggesting that convective heating may be critical as a pilot ignition source. Flame spread rate appears to be primarily governed by factors that affect the intensity of the convective transport. Rapid temporal fluctuations were observed in both radiation and convection, and spectral analysis revealed spectral content at frequencies as high as 50–70 Hz under buoyant flow conditions, and 150–200 Hz under the influence of wind.

Keywords: Discontinuous fuel; Radiative and convective heat transfer

INTRODUCTION

Radiation and convection heat transfer have complimentary roles in wildland fire spread (Anderson, 1969). Their relative contributions depend in a complex way on the prevailing wind speed, fuel distribution, and buoyancy-induced in-drafts. A variety of measurements have been collected from fire experiments including but not limited to flame spread rate (Catchpole et al., 1998; Fons, 1946; Hottel et al., 1965), high-speed photography to determine flame shape (Anderson, 1968), and flame temperature (Anderson, 1968; De Mestre et al., 1989). Various experimental methods have been used to measure the radiation heat transfer. Konev and Sukhinin (1977) used a copper cylinder with a blackened end along with a thermocouple to

Received 1 April 2009; revised 9 February 2010; accepted 14 April 2010.
Address correspondence to Brent W. Webb, Department of Mechanical Engineering, Brigham Young University, Provo, UT 84602, USA. E-mail: webb@byu.edu

measure radiation heat flux. Butler (1993) used both narrow-angle and hemispherical radiometers to measure radiant flux from laboratory fires of poplar excelsior and ponderosa needles under a wide range of conditions (wind and humidity). These data show that flame irradiation is a strong function of flame geometry (length and angle) and fuel conditions.

Laboratory fuel configurations are largely limited to packed fuel beds composed of a variety of different fuel types (Anderson, 1968; Butler, 1993; Catchpole et al., 1993, 1998; De Mestre et al., 1989; Dupuy, 2000; Fons, 1946; Hottel et al., 1965; Konev and Sukhinin, 1977; Pagni, 1972; Santoni et al., 1999; Van Wagner, 1967). Fuel arrays composed of generally homogeneous randomly oriented fuel elements have been shown to provide nominally consistent fire behavior and repeatability. However, the mechanism by which a flame spreads across a gap from one fuel element to another is not well understood.

To the authors' knowledge, no direct–simultaneous measurement of radiation and convection in wildland fires has been reported in the archival literature. Further, the temporal dynamics of the convective and radiative flux have gone unexplored. This work seeks to fill this void through analysis of results from laboratory experiments.

Downloaded By: [Webb, B. W.] At: 18:23 5 October 2010

EXPERIMENTAL METHOD

The primary focus of this effort is to (a) develop a technique for determining experimentally the partitioning between convective and radiative flux in fuel beds consisting of fine wood shavings designed to simulate the discrete fuel spacing found in naturally occurring forest vegetation, (b) measure the temporal dynamics of the convective and radiative flux in this environment, (c) determine the flame spread rate, and (d) determine the frequency content of convection and radiation heat flux in flame spread. These characterizations are sought under different fuel bed configurations, and under both buoyancy- and wind-driven burn conditions.

Sensor Configuration

A two-sensor configuration was used to measure radiation and convection. The sensors were Vatell HFM 7 heat flux microsensors of 6 mm in diameter (sensor active diameter approximately 3.6 mm), and coated with a radiatively absorbent coating ($\varepsilon = 0.94$) and response time 300 μs and frequency response >3000 Hz (Vatell Corporation, 2007). The sensors are equipped with both a thermopile heat flux gage and a resistance temperature sensor, and the voltage from both must be recorded to measure the heat flux. Each sensor was mounted in aluminum cylindrical sensor housings shown schematically in Figure 1a. The mass of the sensor housings is meant to act as heat sink and thus minimize temperature rise and associated radiant emission loss. The sensor housings have a 3.8 cm diameter. The sensors face the same direction and are separated by 5.7 cm. One sensor has a 0.5 mm thick sapphire (transmission range = 0.3–5 μm) window mounted over it, whereas the other sensor is left exposed. The windowed sensor has a 0.5 mm air gap between the sensor face and the window. In this way, the nonwindowed sensor gathers total (convective + radiative) heat transfer whereas the windowed sensor gathers only radiant energy

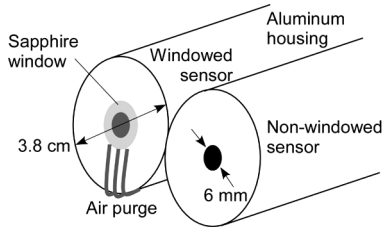

(a)

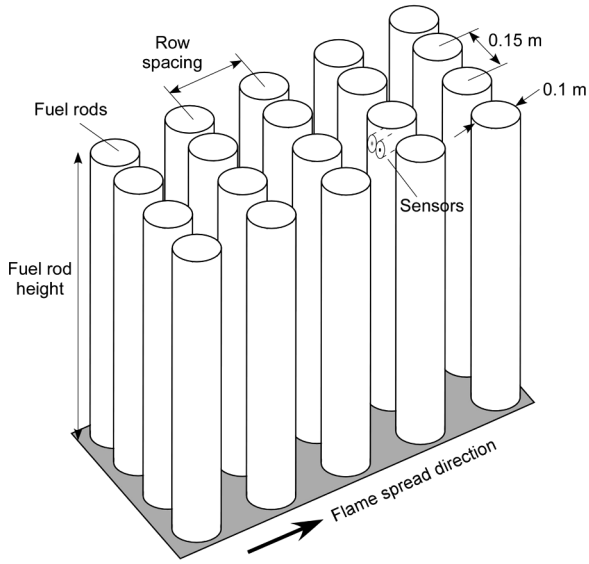

(b)

Figure 1 Schematic illustrations of (a) sensor configuration with windowed sensor on the left and the nonwindowed sensor on the right and (b) discontinuous fuel bed with each cylinder representing a fuel rod for the buoyancy-driven burns.

Downloaded By: [Webb, B. W.] At: 18:23 5 October 2010

(after some loss in transmission through the window). The sensor signals were simultaneously sampled at either 50 or 500 Hz.

The heat flux sensors (unwindowed, as shipped) were calibrated by the manufacturer in a precision blackbody cavity, such that the radiant flux incident on the sensor is known as a function of the imposed blackbody cavity temperature. The calibration equation thus yields the incident radiant flux, $q''_{rad,inc}$, if the sensor is in a radiation-only (blackbody cavity) environment:

$$q''_{cal} = q''_{rad,inc} \tag{1}$$

Only heat flux absorbed by the sensor, q''_{abs}, results in a measurable voltage response, and the absorbed heat flux is a fraction of the flux incident on the sensor, the scaling factor being the emissivity, ε:

$$q''_{abs} = \varepsilon q''_{rad,inc} \tag{2}$$

The difference between the absorbed flux and the incident radiant flux increases with decreasing sensor emissivity; if the sensor emissivity were unity, the absorbed flux would equal the incident radiant flux. Per manufacturer specifications, the sensors respond identically to a given absorbed heat flux, regardless of whether the heating is by radiation or convection. If the sensor is exposed to convective heating or cooling, the sensor calibration provided by the manufacturer yields a flux magnitude higher than that actually experienced by the sensor, by a factor equal to the sensor coating emissivity. Thus, the actual combined convective and radiative flux is always less than or equal to the value indicated by the sensor calibration.

Equations (1) and (2) are general expressions for sensors exposed to convective and radiative modes of heat transfer acting in a combined fashion or independently. The absorbed flux that results in sensor response voltage is related to either the convective, radiative, or combined flux. The nonwindowed sensor used in the experiments reported here responds to both radiation and convection heat transfer, whereas the windowed sensor is not exposed to convective transfer. The heat flux absorbed by the windowed sensor, $q''_{abs,w}$, is equal to the radiant heat flux incident on the outside of the window, $q''_{rad,inc}$, scaled by the emissivity and the effective window transmittance, τ:

$$q''_{abs,w} = \tau\varepsilon q''_{rad,inc} \tag{3}$$

Here it is assumed that the radiant flux incident on both the nonwindowed sensor and the outside surface of the sapphire window (of the windowed sensor) are identical, an assumption validated by controlled tests using the sensor setup described. The effective transmittance of the sapphire window was experimentally measured by igniting 400 g of excelsior strands a distance of 1 m from the windowed and nonwindowed sensors. This distance was selected to insure that no buoyancy-driven flow from the flame would come into contact with the sensors. Thus, both sensors (nonwindowed and windowed) were exposed to the same radiation-only environment. Voltage data were collected for both sensors in this configuration, the calibration fluxes were determined for both sensors ($q''_{cal,w}$ and $q''_{cal,nw}$), and the effective transmittance was determined by calculating the time average of the ratio of the two magnitudes:

$$\tau = average\left(q''_{cal,w}/q''_{cal,nw}\right) \tag{4}$$

Using this method, the value of τ was determined to be 0.62. This value is derived from the mean of over 2,000 measurements taken over 40 s, but due to instrument precision there is some uncertainty. A student's t confidence interval gives 90% probability that the true mean lies between 0.57 and 0.67. Calculating the effective transmittance of the sapphire window allows for the determination of the radiation flux incident on the sensor array.

Substituting Eq. (2) into Eq. (3), and solving for the radiation incident on the outside of the sapphire window yields

$$q''_{rad,inc} = q''_{cal,w}/\tau \tag{5}$$

Downloaded By: [Webb, B. W.] At: 18:23 5 October 2010

The heat flux absorbed by the nonwindowed sensor is the sum of the incident radiant flux that is absorbed and the convective flux:

$$q''_{abs,nw} = \varepsilon q''_{rad,inc} + q''_{conv} \tag{6}$$

where q''_{conv} is the convective heat flux. Substituting Eqs. (2) and (5) into Eq. (6) yields

$$\varepsilon q''_{cal,nw} = \left(\varepsilon q''_{cal,w}/\tau\right) + q''_{conv} \tag{7}$$

Solving Eq. (7) for the convective heat flux yields

$$q''_{conv} = \varepsilon\left(q''_{cal,nw} - q''_{cal,w}/\tau\right) \tag{8}$$

The incident radiation and convection flux can be calculated from Eqs. (5) and (8), respectively, as a function of the calibration heat flux determined from measurements using the nonwindowed and windowed sensors. The convective heat flux values calculated in Eq. (8) are a strong function of the geometry of the sensor housing and should not be interpreted as what a fuel particle with a dissimilar geometry might experience. An attempt to estimate the difference between the convective flux measured and what a fuel element may experience is made in a subsequent section. Despite this limitation, the data provide valuable information regarding the partitioning of convective and radiative flux in a wildland fire environment.

The exposed surface of the window was continuously purged with dried and filtered compressed air. One of the underlying assumptions of the analysis presented previously is that the two sensors are experiencing the same radiative flux environment. This requires that the sensors be positioned physically as close to each other as possible. However, there was risk that the air purge system would interfere with the nonwindowed sensor. For this reason, the experimental setup was tested by activating and deactivating the purge air while the sensors were engulfed in excelsior flames to verify that when the purge air was active, the nonwindowed sensor signal remained unperturbed. Through these tests, the purge air was determined to be both strong enough to keep the window clean and weak enough to ensure that the adjacent nonwindowed sensor signal remained unaffected.

The measurement uncertainty associated with the sensor setup was characterized by sampling noise in a fuel bed before the fuel was ignited. The voltages corresponding to each sensor were recorded and subsequently converted to corresponding values of radiation and convection heat flux. A total of 600 points were sampled, and the precision error associated with this test is estimated to be $\pm 0.32\,\mathrm{kW/m^2}$ for radiation and $\pm 0.34\,\mathrm{kW/m^2}$ for convection with 99% confidence. The bias error associated with these measurements is minimized by adjusting the voltage output of the sensors after amplification to a mean of zero when the sensors have reached thermal equilibrium with the burn chamber.

Fuel Bed Assembly

As mentioned previously, most experimental fires directed at simulating wildland flames consist of a thin bed of continuous fuel (Butler, 1993; Catchpole et al.,

Downloaded By: [Webb, B. W.] At: 18:23 5 October 2010

1998; De Mestre et al., 1989; Fons, 1946; Konev and Sukhinin, 1977; Pagni, 1972; Telisin, 1973; Van Wagner, 1967). These continuous fuel experiments have merit in that they create a steadily spreading flame front, thus removing variability from the experiment. However, they likely do not accurately represent most wildfire environments in which fuel is distributed in discrete elements or clumps. It is of interest to simulate less continuous fuels. This was accomplished by wrapping shredded aspen (*Populus tremuloides*) heart wood (commonly termed excelsior) around a steel rod, thus creating a roughly cylindrical fuel rod with a diameter of approximately 0.1 m. The height of the fuel rods was either 0.61 or 1.22 m. A total of 120 g ($\pm$4 g) of fuel was wrapped on the 0.61 m high fuel rods, and that amount was doubled for the 1.22 m high fuel rods. The fuel rods were then arranged laterally in rows of four with a 0.15 m distance between the centers of adjacent fuel rods in each row, as shown schematically in Figure 1b. This spacing was chosen so the fuel rods would be close enough to ensure that the entire row would ignite rather than the ignition of each fuel rod in the row occurring separately. The spacing between rows was varied from 0.15, 0.20, or 0.25 m (fuel rod center-to-center spacing). In this way the fire intensity of each experiment could be varied. A fuel row spacing of 0.15, 0.20, and 0.25 m corresponds, respectively, to a fuel loading of 5.3, 4.0, and 3.2 kg/m^2 for the 0.61 m fuel rods. Fuel row spacings of 0.20 and 0.25 m yield 8.0 and 6.4 kg/m^2 fuel loading, respectively, for the 1.22 m fuel rods. The flame intensity was influenced not only by changing the fuel height but also by introducing forced flow of air simulating wind-driven combustion conditions.

The excelsior was conditioned at 291 K and 35% relative humidity for 8 hr to achieve a moisture content of approximately 7–8% (oven-dried basis). The heat flux sensors were mounted on one of the center two fuel rods far enough downstream in the flame spread direction so that a steady rate of spread could be achieved before the flame arrived at the sensors. The sensor housing was positioned with sensor faces nominally flush with the excelsior fuel, oriented toward the oncoming flames, and were positioned at a height of 0.53 m from the floor of the fuel bed for all experiments. This placed the sensors near the top of the 0.61 m high fuel rods, and near the middle of the 1.22 m high fuel rods. The sensor leads were routed behind the sensors and out of the fuel bed to the data acquisition system. A digital videocamera oriented to give a side view of the sensors created a visual record of each experiment, and documented flame impingement on the sensor face and other combustion events.

The flame spread rate (in rows/s) was calculated by reviewing the videographic record of each burn, and measuring the time between ignition of adjacent fuel rows. The known fuel row spacing was then used to calculate the flame spread rate (m/s). The flame spread rates calculated for all rows in a given experiment were averaged to characterize the spread rate for that experimental condition. A fuel row-based spread rate (rows/s) was also determined by multiplying the elapsed time for a given data set.

Once the fuel bed was assembled and conditioned, the experiment commenced by spraying approximately 40 cc of ethanol on the lower 5 cm of the first row of fuel and then igniting it. The ethanol ensured that the entire base of the first row ignited at the same time. Experiments were conducted both in a wind tunnel and in a quiescent environment. The total length of the fuel bed was 1.22 m in the experiments conducted in the quiescent environment. The fuel bed length was 6.1 m long in the wind

Downloaded By: [Webb, B. W.] At: 18:23 5 October 2010

Table 1 Experimental conditions investigated and corresponding measured flame spread rate

Fuel height (m)	Row spacing (m)	Fuel loading (kg/m^2)	Condition	Spread rate (m/s)
0.61	.15	5.3	Buoyancy-driven	.016 (.11 rows/s)
	.20	4.0	Buoyancy-driven	.012 (.060 rows/s)
	.20	3.2	Wind-driven, 2.2 m/s	.080 (.40 rows/s)
1.22	.20	8.0	Buoyancy-driven	.017 (.080 rows/s)
	.25	6.4	Buoyancy-driven	.018 (.070 rows/s)

tunnel experiments to permit establishment of steady flaming in the wind-assisted combustion environment. The heat flux sensors were positioned in the same lateral position relative to the fuel bed width in both the buoyancy-driven and wind-assisted burn tests. A single wind tunnel speed of 2.2 m/s (centerline speed) was investigated. The burn chamber used to conduct buoyancy-driven experiments was 20.1 m high with a floor that was 13.4 m square. The wind tunnel has a test section that is 7.5 m long in the streamwise direction, 3.3 m wide, and 3.3 m high. Catchpole et al. (1998) provided additional details about the facility. Table 1 shows a summary of experimental conditions investigated, and spread rates calculated from the videographic record of each experiment.

Downloaded By: [Webb, B. W.] At: 18:23 5 October 2010

RESULTS AND DISCUSSION

Temporal Characteristics of Heat Flux

A plot of the representative measured radiation and convection flux history from these experiments is shown in Figure 2. These data come from a buoyancy-driven flow experiment with 0.61 m high fuel rods and 0.20 m row spacing. The sampling rate used for this experiment was 50 Hz. The general features of the combustion behavior are discussed here.

The time-series heat flux data of Figure 2a reveal radiative heating is detected well ahead of the convective flux, evidenced by the rise in radiative heat flux 45 s before the nonzero convective heat flux detected. The videographic record of the experiment revealed that when the sensor is engulfed in flames the convection heat flux manifests an abrupt and significant rise with peaks indicating intense heating. This sharp rise in convective flux is hereafter arbitrarily assigned a time of zero. The data of Figure 2a manifest local maxima in radiation heat flux at −63, −43, −25, and −5 s. The time elapsed between the peak of one local maximum to the next (∼20 s) corresponds nominally to the elapsed time between observation of a sustained flame on one fuel row and its establishment on the next row. As is demonstrated later, this apparent periodicity in the radiation flux is observed only in experiments characterized by sufficiently large fuel rod row spacing to cause the ignition and combustion to occur as relatively discrete events. The sensors experience convective cooling in this configuration 25–30 s before the sensors are engulfed in flames. This convective cooling is a result of radiative preheating of the sensors prior to the arrival of the flame and buoyancy-induced in-draft of cool air. This cooling trend prior to onset of combustion is interrupted by discrete heating events in the

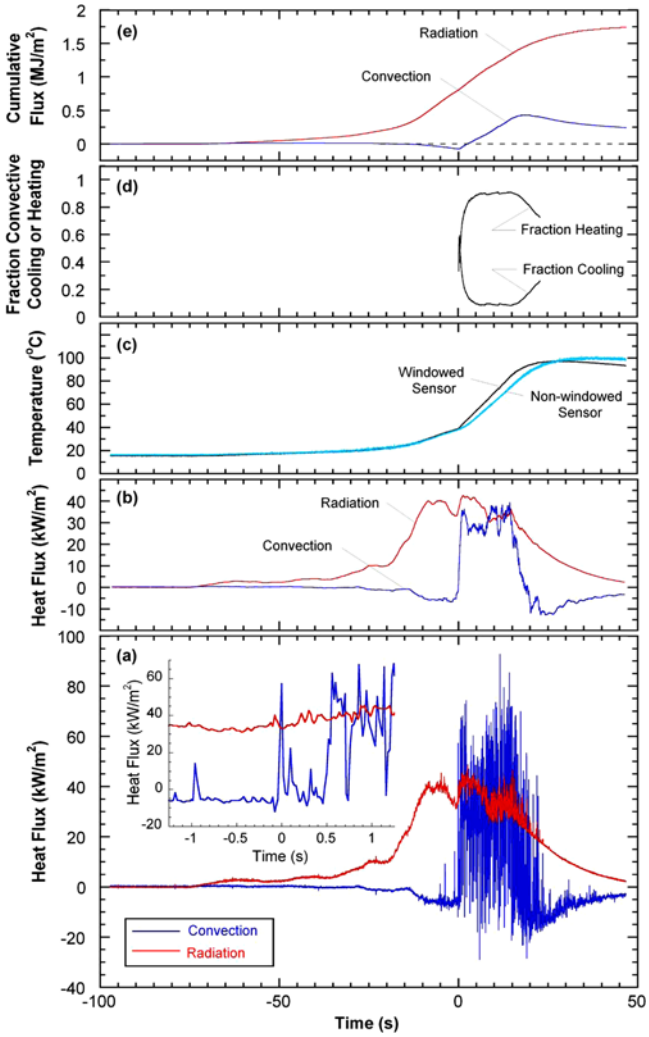

Figure 2 Measured radiation and convection characteristics for 0.61 m fuel rods and 0.20 m row spacing: (a) radiation and convection heat flux, (b) heat flux histories filtered with 1-s moving window average, (c) sensor temperatures, (d) fraction of time convective cooling and heating after flame arrival (time = 0 s), and (e) cumulative flux.

time period nominally 5 s prior to ignition. However, the negative convective heat flux is not observed in all experiments.

The inset panel of Figure 2a shows an expanded time scale for a 2.5-s period around ignition. The convective and radiative flux data were collected in this experiment at 50 Hz. The panel illustrates short convective pulses preceding the full combustion event. These pulses may be intermittent flame bursts sweeping past the sensors, and suggest that convection of combustion products are a mechanism for ignition. At time 0 s a significant rise in the convective flux reaching a magnitude of approximately 60 kW/m^2 is observed. This peak is of short duration, however,

Downloaded By: [Webb, B. W.] At: 18:23 5 October 2010

and the convective flux drops to a near-zero value followed by heat flux excursions reaching magnitudes of 10–20 kW/m^2. The inset panel illustrates clearly the rapid temporal fluctuations of convective heating, with strong pulses followed by abrupt drops in the flux occurring on a time scale of the order of 0.02–0.05 s. These fluctuations are believed due to pockets of alternately hot combustion products and cool ambient air sweeping past the sensors.

The radiation heat flux transients in Figure 2a peak at nearly 50 kW/m^2, whereas the maximum in the convection heat flux transients are approximately 90 kW/m^2. The radiative flux rises nearly monotonically, with relatively small temporal fluctuations in its magnitude through the combustion event. This may suggest that the flame is relatively optically thick, such that any local temporal fluctuations in flame temperature and emitting constituents are compensated by flaming combustion elsewhere, and do not appreciably affect the radiation flux history. By contrast, after the arrival of the flame, the temporal fluctuations in convection heat flux become rapid and dramatic, ranging between -30 and 90 kW/m^2. As observed previously, these fluctuations suggest the existence of alternating packets of hot combustion gas and cold ambient air while the sensors are engulfed in flames. The fluctuations occur on a time scale as low as 0.05 s, and the frequency content is explored in a subsequent section. These fluctuations occur at considerably higher frequencies than has been traditionally associated with wildland fire.

In an effort to see more clearly the trends in the rapidly fluctuating heat flux signals, a moving window averaging filter of window size 1 s was applied to the flux histories of Figure 2a. The filtered convective and radiative heat flux data are shown in Figure 2b. Because the fluctuations in radiative flux are small, there is only modest difference between the unfiltered and filtered radiation signal. However, the difference in unfiltered and filtered convective flux highlights the rapid fluctuations in convective heating of the sensors. The filtered data of Figure 2b show that for this experimental condition the radiation flux generally exceeds the average convective flux through most of the event.

The temperature history of both heat flux sensors is shown in Figure 2c. The sensor temperature data reveal a rise corresponding to the onset of the radiation heating. The sensors' temperature increases monotonically through the combustion event, reaching a maximum for this test of approximately 100°C. This is representative of all tests; the maximum sensor temperature observed in all experiments was 120°C. It may be argued that relative to the high-temperature combustion gases, the sensors are very nearly at ambient temperature. Further, the maximum temperature of the sensors results in a radiant heat loss from the sensors of less than 1.1 kW/m^2, which is no more than 2% of the 50 kW/m^2 peak radiation flux.

Figure 2d illustrates the running fraction of time during the combustion event that the convective heat flux exceeds 1 kW/m^2 and falls below -1 kW/m^2, termed *fraction heating* and *fraction cooling*, respectively. These are computed beginning at flame arrival (time = 0 s). This temporal fraction of convective cooling/heating is determined by accumulating the number of data points above and below the ± 1 kW/m^2 convective heating/cooling threshold in the time record. This parameter is presented to characterize both positive (heating) and negative (cooling) fluctuations in the convective flux history. The data reveal that the convective transients heat the sensors approximately 75–90% of the time during the event. Quite

Downloaded By: [Webb, B. W.] At: 18:23 5 October 2010

surprisingly, the sensors are exposed to cooler gases 10–25% of the burn event, resulting in negative convective flux. These data highlight the rapid transients of positive and negative excursions in the convective flux during combustion events.

The burn event of Figure 2a, defined loosely as the time from first indication of radiation flux to that corresponding to a return to zero-flux conditions, is of duration approximately 120 s. The actual combustion event during which flame engulfs the fuel rod on which the sensors are mounted lasts between 20 and 25 s. After the combustion event, both radiation and convective flux decay to zero as the hot fuel bed cools and the embers burn out, and the sensors cool to ambient temperature. While the nonzero radiation flux that prevails following the combustion event is indicative of clear exposure to a hot radiating environment, the decay in negative connective flux that occurs at approximately 22 s is reflective of the thermal mass of the sensor and sensor housing, which cool while exposed to ambient air.

Figure 2e illustrates the cumulative behavior of the radiative and convective heat flux experienced by the sensors as calculated by a running integration of the time-resolved heat flux over time. The data reveal that the cumulative radiative flux (or total heat load experienced by the sensors) rises slowly and quite modestly prior to flame arrival. Consistent with the convective cooling noted in the temporally resolved flux data of Figure 2a, the cumulative convective flux drops below zero prior to flame arrival, rises to a peak after onset of combustion, and falls due to cooling of the heated sensor and housing following the combustion event. The magnitude of the cumulative radiation flux is four to five times that of the convective flux for this experimental condition. Despite the dominance of radiation heat transfer indicated in Figure 2e, the time-series data of Figure 2a suggest that ignition may be a convection-driven event as packets of hot combustion products are swept past the downstream rows.

Although the flames by nature are highly turbulent, the experiments were found to be quite repeatable. Experiments were repeated for all experimental conditions investigated, with the results reported elsewhere (Frankman, 2009). Although turbulent variations in radiative and convective flux magnitude were clearly present, the general and distinctive features of the burn were similar in all repeated tests. Maxima and minima in heat flux magnitudes for the repeated tests were remarkably close. Temporal variations in measured sensor temperatures were generally within ± 12 K. In this study a single representative data set from repeated tests at identical experimental conditions is presented for analysis and discussion.

It must again be acknowledged that the convective flux reported here cannot be interpreted as the convective flux experienced by the fuel elements. Convective heating and cooling is a strong function of both object geometry and temperature. The convective flux reported here is that flux which is experienced by the sensor and housing used in the experimental measurements. The difference between the measured convective heat flux and that experienced by the fuel elements was quantified by modeling the heat transfer experienced by the sensor and that by a simulated fine fuel element under identical conditions. The parameters of the study were intentionally chosen to be the most extreme to reflect a worst-case scenario of convective cooling or heating. The disc-shaped sensor is assumed to be subject to direct impingement of hot combustion or cool ambient air of known freestream velocity. The fuel is assumed to be cylindrical and experiencing crossflow heat transfer at a

Downloaded By: [Webb, B. W.] At: 18:23 5 October 2010

freestream velocity identical to that which the sensor experiences in direct impingement. Accepted empirical correlations for the heat transfer coefficient in impingement flow (Jakob, 1949) and cylinder crossflow (Churchill and Bernstein, 1977) heat transfer were used in the heat transfer calculations. The results of the study are shown in Figures 3a and 3b, which show the convective heat flux when the fuel and the sensor are heated and cooled, respectively. During heating, the temperature of the sensors and the fuel are assumed to be at their minimum possible value, 300 K. A flame temperature of 1600 K is used in the heating calculations, again assuming a worst-case scenario, well above the peak combustion temperatures measured in crown fires (Butler et al., 2004). During cooling, the sensors and fuel are assumed to be at their maximum possible values. The maximum values are 423 K for the sensor (measured experimentally), and the nominal minimum ignition temperature for woody fuels, 523 K (Babrauskas, 2003). Again, these temperatures were chosen to simulate the most extreme heating or cooling conditions. The analysis results shown in Figure 3 reveal that even under these extreme conditions, the magnitude of the absolute heat flux measured by the sensor is always less than that which would be experienced by a cylindrical fine fuel particle under both heating and cooling conditions. The modeled difference in heat flux magnitude experienced by sensor and fuel can reach over 200%, with the difference increasing with smaller diameter fuels.

Downloaded By: [Webb, B. W.] At: 18:23 5 October 2010

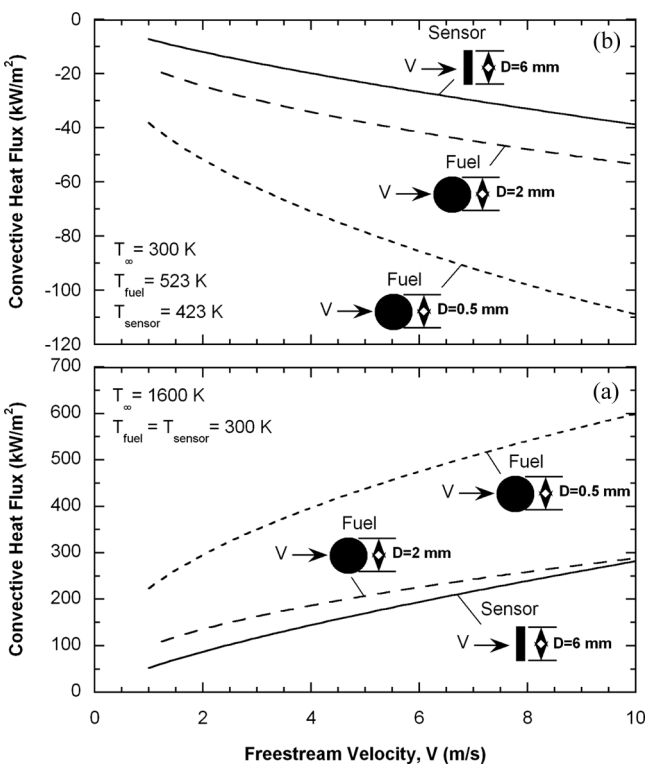

Figure 3 Comparison of the modeled heat flux experienced by the sensor and fuel element: (a) convective heating and (b) convective cooling.

These trends were verified for fine fuels of diameter as large as 3 mm. It is thus concluded that fine fuels probably experience a more extreme convective heat flux magnitude than the sensor measurements reported here.

Three parameters were varied in the laboratory experiments: fuel row spacing, fuel height, and ambient air speed (wind or no wind). The effect of these parameters on burn characteristics is now explored.

Figure 4 illustrates convection and radiation heat flux data for two experiments with the large fuel height (1.22 m), but with different row spacing—0.20 m and 0.25 m. Figure 4a reveals that the peak radiation flux is higher for the smaller fuel rod row spacing (0.20 m). It is also of note that temporal fluctuations in the convective flux are characterized by higher amplitude for larger row spacing (0.25 m), and the time period of intense convection heating is of longer duration for this row spacing. Further, negative convective flux (preignition cooling) prior to flame arrival is observed only for the larger fuel row spacing. In other words, more compact fuel beds apparently have the effect of suppressing buoyancy-induced ambient air flow prior to flame arrival. Further, the larger fuel row spacing allows greater visibility

Downloaded By: [Webb, B. W.] At: 18:23 5 October 2010

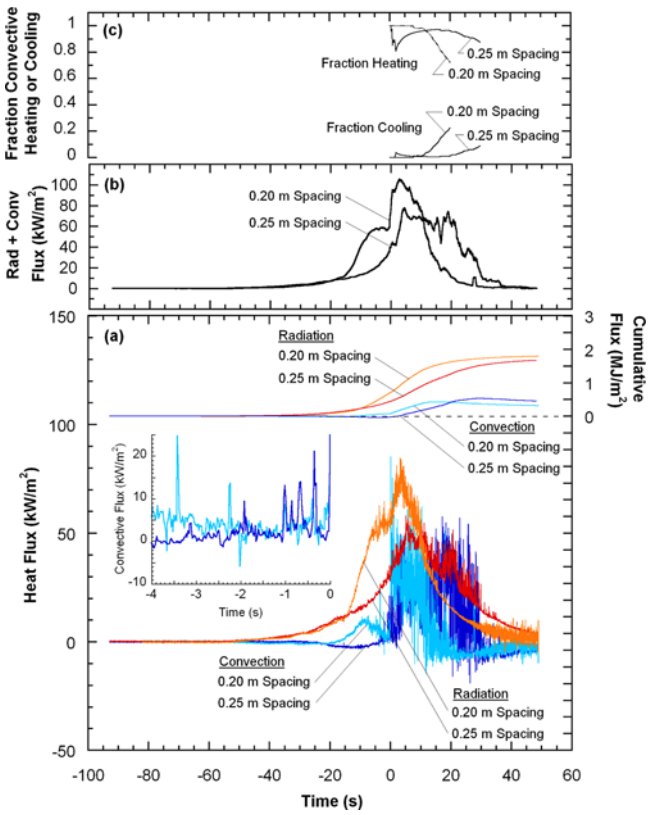

Figure 4 Comparison of radiation and convection for two burns with the same fuel height (1.22 m) but with different row spacing (0.20 and 0.25 m): (a) radiative and convective flux, and cumulative flux; (b) total (radiative + convective) flux filtered with 1-s moving window average; and (c) fraction of time convective cooling and heating.

of the approaching flame and greater opportunity for ambient air to penetrate the bed. As illustrated in the inset panel of Figure 4a showing the convective flux for the time period 4 s before the full onset of flaming, short-duration convective heating pulses are also observed shortly before ignition for both experimental configurations, again supporting the idea that ignition may ultimately result from convection events.

The cumulative convective flux data for the experimental configurations displayed in Figure 4a for a fuel height of 1.22 m are similar to those seen in Figure 2 for the shorter 0.61 m fuel height. Figure 4 shows that the cumulative flux for the larger row spacing (0.25 m) ultimately exceeds that observed in the smaller row spacing (0.20 m). It appears that the convective heat load on the sensors is greater for the smaller fuel row spacing at increasing fuel heights. Moreover, the radiative flux for the larger fuel height exhibits a higher cumulative magnitude throughout the burn event for the smaller row spacing.

Figure 4b shows the total (radiative + convective) flux history using a 1-s moving window average for the 1.22 m fuel height at both 0.20 and 0.25 m fuel row spacings. The data show that the 0.20 m spacing yields greater total flux early in the event due to its higher radiative flux in this period, whereas the 0.25 m spacing exhibits greater total flux in the latter part of the event because of extended duration of high intensity convective flux. Note from Table 1 that the flame spread rate is only slightly higher for the 0.25 m row spacing at this fuel height (and may be within the uncertainty of the flame spread calculations), despite the higher peak radiative, cumulative, and total flux for the 0.20 m row spacing configuration. It may be that the spread rate is more strongly linked to the higher intensity, longer duration convective heat transfer seen in the larger row spacing experiment. These observations are supported by the fraction heating data of Figure 4c in which the 0.25 m row spacing shows longer duration heating than the case of 0.20 m spacing. Further, the 0.20 m spacing has significantly higher magnitude and longer duration fraction cooling.

Figure 5 illustrates the effect of fuel rod height on the heat transfer behavior. This figure compares flux histories for two experiments with the same row spacing of 0.20 m, but with different fuel heights (0.61 and 1.22 m). The 1.22 m high fuel rod configuration has both twice as much fuel to burn per unit area and a faster spread rate (see Table 1), and thus exhibits the more intense combustion. This is seen in the significantly higher peak radiation flux for the 1.22 m high fuel rod configuration. In the lower intensity 0.61 m high fuel rod experiment, the radiation flux is detected earlier and well ahead of the flame front with local maxima seen in the data corresponding to discrete combustion events of upstream fuel rods mentioned previously, all of which can be explained by the difference in spread rate summarized in Table 1 for the two experiments. The flame spread rate for the 1.22 m fuel height is roughly 50% higher than that for the 0.61 m fuel height, perhaps due to the presumed greater intensity of buoyancy flow and resulting convective driving force for the larger fuel height. It is seen that the convection heat flux is negative before flame arrival with the exception of the short duration positive convective pulses for the 0.61 m fuel height. The higher intensity 1.22 m high fuel rod experiment shows no local maxima in radiation prior to ignition and exhibits a positive convective heat flux just before flame arrival. After flame arrival the 0.61 m high fuel rod experiment shows a lower radiation heat flux peak and lower amplitude temporal fluctuations in the convective

Downloaded By: [Webb, B. W.] At: 18:23 5 October 2010

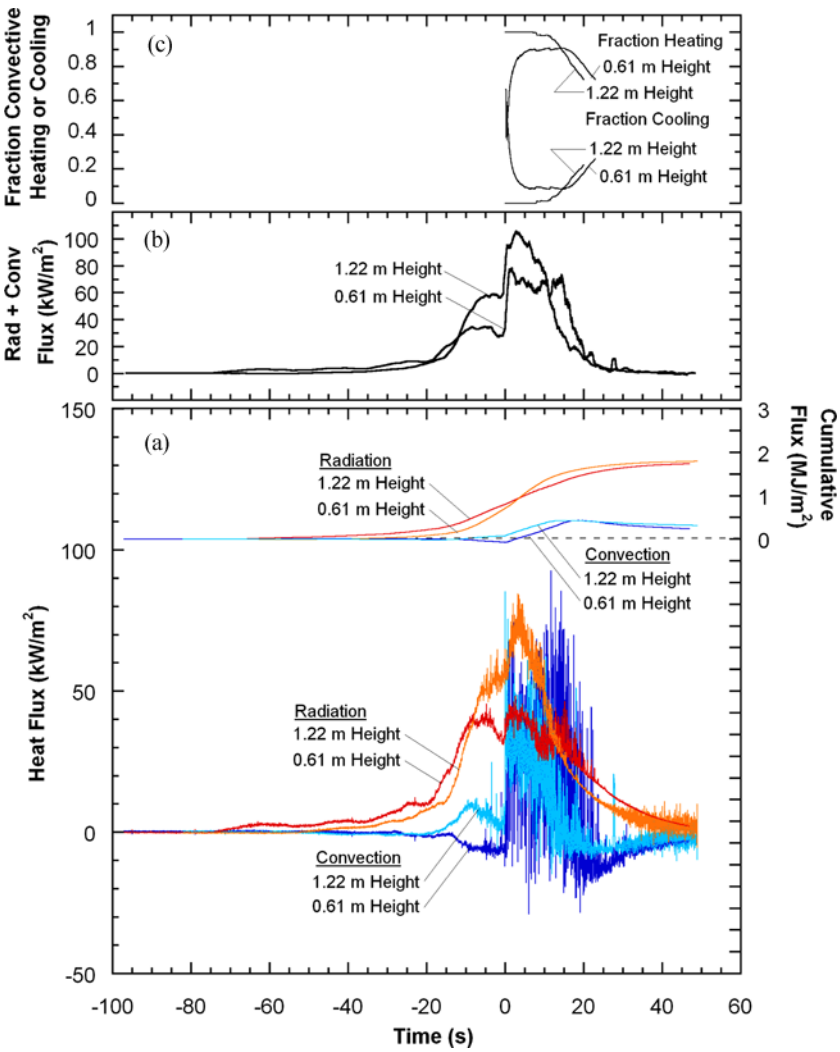

Figure 5 Comparison of radiation and convection for two burns with the same row spacing (0.20 m) but with different fuel heights (0.61 and 1.22): (a) radiative and convective flux, and cumulative flux; (b) total (radiative + convective) flux filtered with 1-s moving window average; and (c) fraction of time convective cooling and heating.

heat flux. Convective flux data for both experimental configurations exhibit the short-duration heating pulses prior to full-onset combustion that has been observed previously.

The cumulative convective and radiative flux levels are not significantly different for the two different fuel heights shown in Figure 5. The cumulative radiative flux for the smaller (0.61 m) fuel height rises more slowly than the larger (1.22 m) height, but the peak magnitude is slightly higher for the 0.61 m height configuration, this despite the fact that the fuel density (per unit plan area) is twice as high in the

Downloaded By: [Webb, B. W.] At: 18:23 5 October 2010

Figure 6 Photograph of fuel bed burned in the presence of wind at 2.2 m/s.

Downloaded By: [Webb, B. W.] At: 18:23 5 October 2010

1.22 m fuel height test, suggesting that increasing fuel load does not necessarily correspond to increased heating magnitude.

The effect of wind-driven combustion was investigated by performing experiments in a wind tunnel, illustrated photographically in Figure 6. The fuel bed for the wind-driven burn test was longer (6 m) than the buoyancy experiments to allow the fuel to reach a steady rate of spread before reaching the sensors. As seen in the photograph, the forced air flow has the effect of inclining the flame such that the flame extends above the fuel bed well ahead of the fuel rod combustion zone. Figure 7 shows temporal heat flux behavior from two experiments with the same row spacing (0.20 m) and fuel height (0.61 m), where one experiment was conducted in a quiescent environment and the other burned with a 2.2 m/s wind. The measured peak sensor temperature (not shown) was lowered from 100°C in the buoyancy-driven burns to 45°C for the wind-driven configuration. Figure 7 shows quite clearly that the peak radiation flux in the wind-driven burn data is more than twice that of the buoyancy-driven configuration. Radiation is detected in the buoyancy-driven burn experiment well ahead of flame arrival, whereas relatively, its influence is delayed in the wind-assisted combustion. Both the wind- and buoyancy-driven experiments exhibit modest convective cooling before flame arrival. As illustrated in the inset panel of Figure 7 showing a 5-s period, strong short-duration convective pulses occur immediately prior to ignition for both configurations. The wind-driven burn data exhibit a more gradual transition to the strongly fluctuating flux condition characteristic of full combustion.

Figure 7 shows that the postignition transients in convective heat flux exhibit peak magnitudes exceeding 90 kW/m^2 for both experimental configurations. However, the wind-driven burn convective flux is characterized by smaller maximum-to-minimum excursions in the temporal fluctuations than the buoyancy-driven burn. This is further illustrated by the fraction of convection heating and cooling data plotted in Figure 7c, which shows that immediately after flame arrival (0–5 s) there

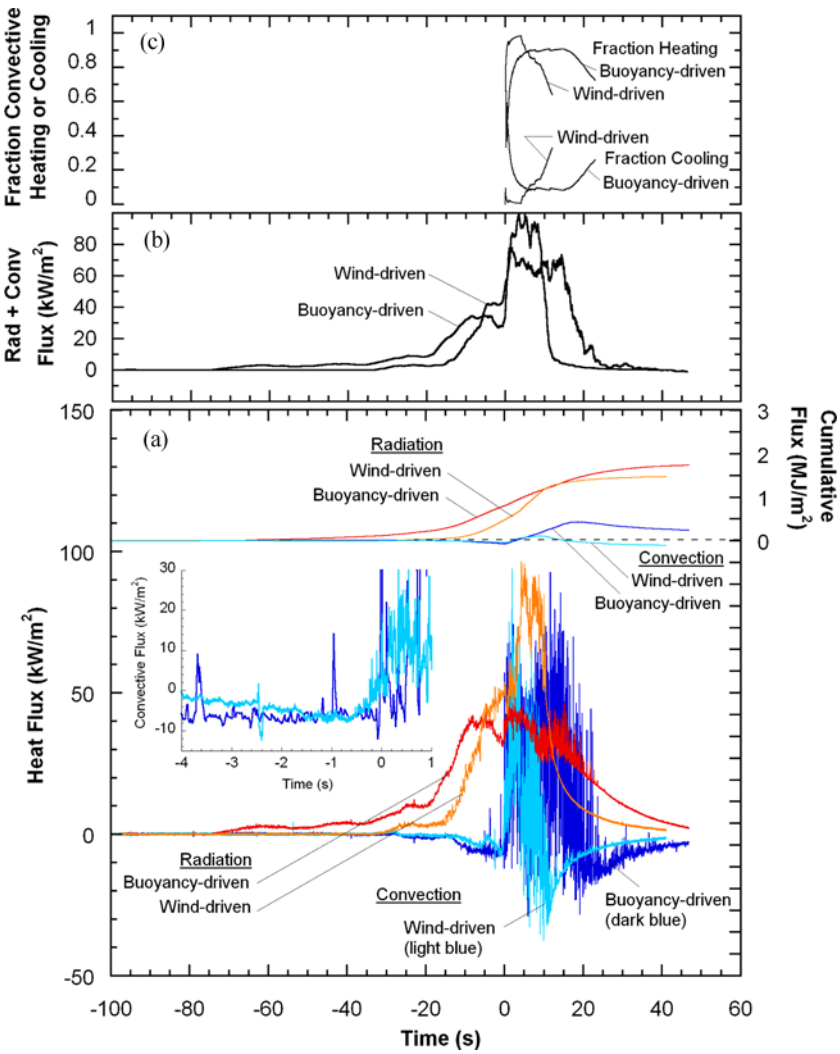

Figure 7 Comparison of flux histories for two experiments with the same fuel height (0.61 m) and row spacing (0.20 m), one buoyancy-driven and the second wind-driven with a 2.2 m/s crossflow: (a) radiative and convective flux, and cumulative flux; (b) total (radiative + convective) flux filtered with 1-s moving window average; and (c) fraction of time convective cooling and heating.

is little convective cooling in the wind-driven experiment, whereas considerable negative convective flux is evident during this time period in the buoyancy-driven experiment. By contrast, the fraction heating shortly after ignition is considerably higher for the wind-assisted burn configuration. It may be suggested that the forced flow provides more effective delivery of oxygen for combustion, and suppresses the large-amplitude turbulent convective fluctuations evident in buoyancy-driven combustion. Despite the more effective delivery of oxygen in the wind-driven experiment, the cumulative radiative and convective flux levels are consistently higher in the

Downloaded By: [Webb, B. W.] At: 18:23 5 October 2010

buoyancy-driven burn configuration, due in large part to the longer duration of the heating event. The cumulative convective flux is positive only for a small portion of the wind-driven burn, indicating significant convective cooling of the sensors. This may suggest that the minimum heating magnitude and rates needed for ignition are substantially lower than those observed, and that ignition is primarily influenced by convectively driven events.

The total (radiation + convection) flux data computed using a 1-s moving window average are shown in Figure 7b. The peak total flux is higher for the wind-driven configuration, but the duration of the burn event is shorter. As seen in Table 1, the flame spread rate for the wind-driven burn is a factor of six times that of the buoyancy-driven burn for the same fuel height and row spacing. This cannot be explained either by the differences in cumulative or total flux for these two burn configurations, but seems more clearly tied to the strength of the convective flow. The significantly higher flame spread rate for the wind-driven burn observed for the conditions of Figure 7 provide further support for the suggestion that ignition (and hence, flame spread) is primarily a convection-driven phenomenon.

The flame spread rate of the two experimental conditions in Figure 7 is so different that it is difficult to determine if the radiation detected by the sensors well before ignition originates from the flames above the fuel bed or from the combusting fuel bed itself. It is instructive to register the flux detected by the sensors to the location from which the flame originates measured by row number upstream of the sensor location. To that end, the temporal behavior of the different burn configurations was normalized by plotting the convective and radiative heat flux histories as a function of the position of the combustion zone (fuel row), determined from the fuel row-based flame spread rate rather than elapsed time. This permits interpretation of the combustion history in terms of the flame location. Figure 8 reproduces the data of Figure 7 with the flux histories plotted as a function of combustion zone position rather than time. Row 0 represents the fuel row where the sensors are located. The heat flux associated with Row -1 indicates the flux level when the flame is one row immediately upstream of the sensors. The data of Figure 8 indicate that the radiation heat flux in the wind-driven experiment is detected when the flame is 11 rows upstream of the sensor location. With 10 unignited rows of fuel between the sensor and the burning fuel, it is unlikely that the radiation detected by the sensor is transmitted through the fuel bed. Rather, the sensor is viewing the wind-angled flames above the fuel bed downstream of the combustion zone. Although it is true that radiation is detected from the flames, the magnitude of this radiation remains below $5\,\mathrm{kW/m^2}$ until the flame zone reaches the sixth fuel row upstream of the sensor. Prior to this, the sensors see relatively weak, intermittent flames visible above the fuel bed. As the flame moves nearer the sensor location, the flame is more intense and occupies a greater portion of the sensor's hemispherical field of view. By contrast with the early detection of radiation flux in the wind-driven burn, the radiation flux for the buoyancy-driven burn is detected only when the flame zone reaches a position approximately 4 rows upstream of the sensor location. A large increase in the radiant flux occurs when the flame zone is 1 row from the sensors. It is important to note that the radiation flux for the wind-driven burn configuration exceeds $25\,\mathrm{kW/m^2}$ even when the flame zone reaches a position 5 rows beyond the sensor location, whereas the radiation flux has dropped below $25\,\mathrm{kW/m^2}$ in the buoyancy-driven burn when

Downloaded By: [Webb, B. W.] At: 18:23 5 October 2010

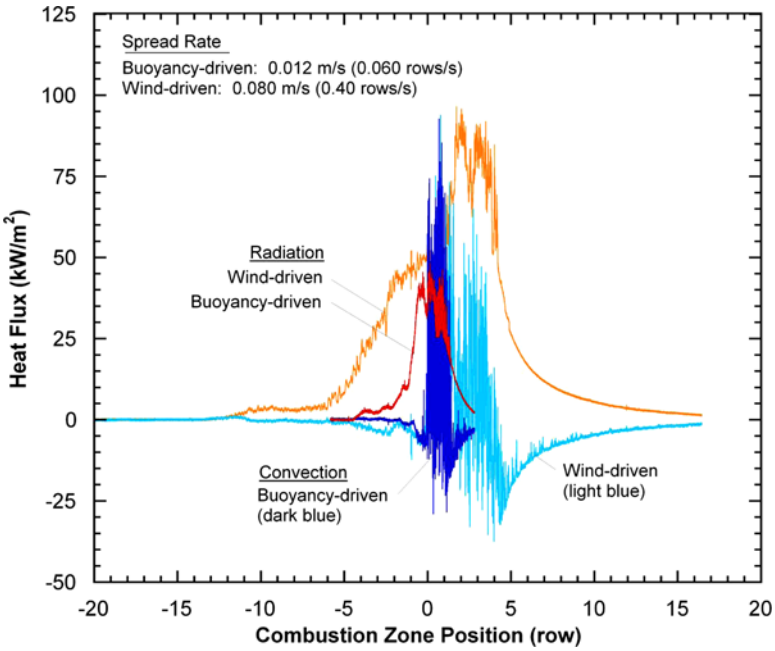

Figure 8 Radiation and convection heat flux histories for buoyancy- and wind-driven burns with 0.61 m fuel height and 0.20 m row spacing plotted as a function of combustion zone position.

the flame has spread 1 row beyond the sensor location. This suggests that the combustion zone in the wind-driven burn is considerably longer than in the buoyancy-driven burn. The crossflow apparently stretches the combustion zone across several rows as the flame spreads from one row to another.

Figure 9 reproduces the data of Figure 5, plotted as a function of combustion zone position (in rows) rather than time. Both experiments feature the same row spacing (0.20 m) but with differing fuel rod heights—0.61 and 1.22 m. Radiation heating is detected when the flame reaches the same nominal upstream location (expressed in rows) for both experiments. Recall that the sensors are located at the same vertical position near the middle of the fuel rod height for the 1.22 m fuel beds and near the top of the fuel bed for the 0.61 m fuel rod. Thus, the view of the flames above the fuel bed is restricted for the 1.22 m fuel height. Given that the sensors detect radiation heat flux when the flame is at the same position relative to the sensors for both experiments, and further, that the sensors can view the flames in the 0.61 m fuel rod height experiment and not the 1.22 m fuel rod height experiment, it would seem that flame radiation (from flames extending above the fuel) in the buoyancy-driven experiment is low. Only when the flame is within 1 row of the sensors does the radiation flux from the 1.22 m fuel height configuration exceed that of the 0.61 m height burn. Both sets of data exhibit the short-duration convective heating pulses immediately prior to ignition, and both are seen to occur when the combustion zone is within a half-row of the sensor location, further supporting the assertion that the convective heating pulses provide the pilot ignition mechanism for flame spread from one row to the next.

Downloaded By: [Webb, B. W.] At: 18:23 5 October 2010

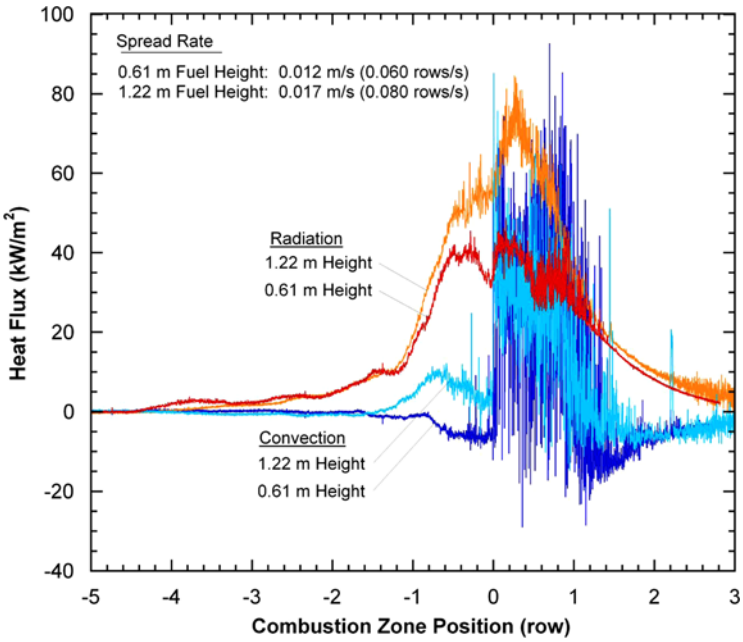

Figure 9 Radiation and convection heat flux histories for 0.20 m row spacing and 0.61 and 1.22 m fuel height in the buoyancy-driven experiments plotted as a function of combustion zone position.

Downloaded By: [Webb, B. W.] At: 18:23 5 October 2010

From the aforementioned plots, it is suggested that convective heating or cooling is significantly lower in magnitude than the energy delivered through radiant energy transfer prior to ignition. However, there are indicators that intermediate very short-duration convective heating pulses occur immediately in the few seconds preceding ignition, suggesting that intermittent flame presence may be critical, possibly as a pilot ignition source and a primary mechanism for flame spread.

Spectral Analysis

In an effort to characterize the difference in temporal fluctuation intensity between radiation and convection heat flux under different experimental conditions, the frequency content of the time-series data in experiments where the flux was sampled at 500 Hz was determined by the use of a Fast Fourier Transform (FFT). The data processed in the FFT included the time period beginning with the first nonzero radiative and convective flux and ending with the conclusion of the postflame cooling period. Figure 10 shows the heat flux power spectrum for radiative and convective flux data collected at four different experimental conditions. No signal conditioning was performed as part of the analysis. Figure 10a presents data from a buoyancy-driven experiment with a 0.61 m fuel height and 0.15 m row spacing. The data of Figure 10b are also from a buoyancy-driven experiment, but with 0.61 m fuel height and 0.20 m row spacing. Figure 10c is again from a buoyancy-driven experiment but with 1.22 m fuel height and 0.20 m row spacing. Finally, Figure 10d is from a wind-driven experiment with 0.61 m fuel height and 0.20 m

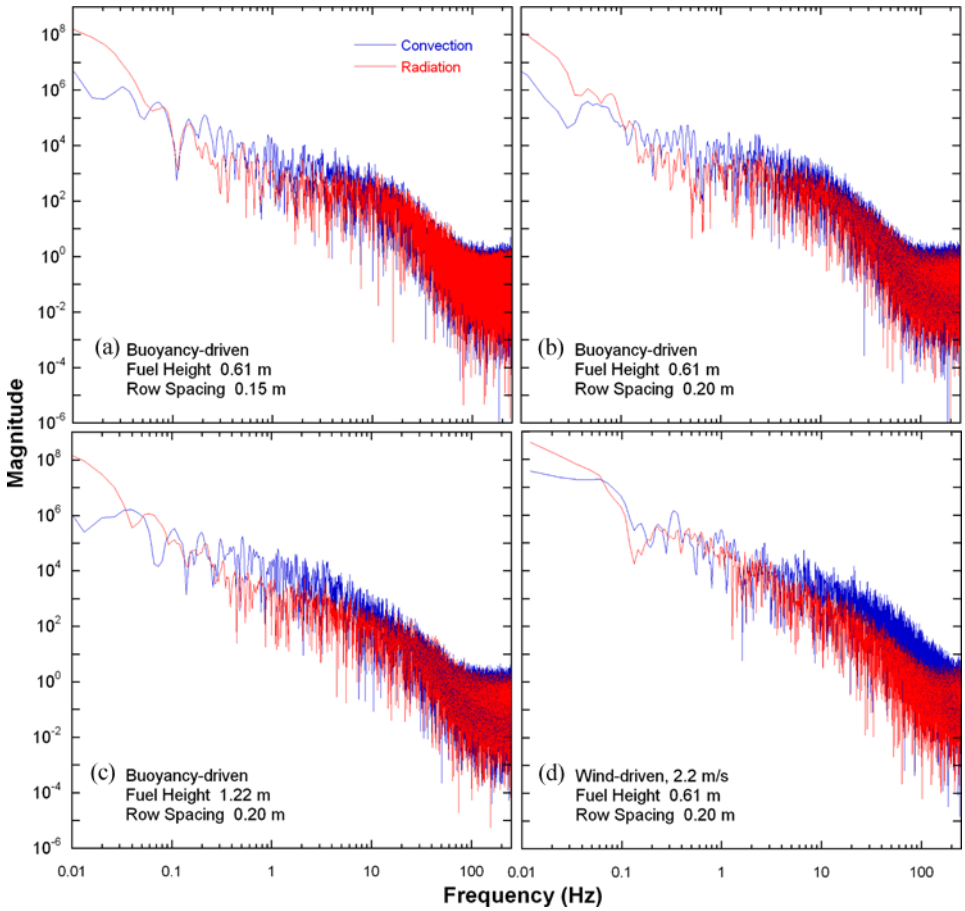

Figure 10 Power spectra for fluctuating convection and radiation heat flux: (a) buoyancy-driven burn, 0.61 m fuel height and 0.15 m row spacing; (b) buoyancy-driven burn, 0.61 m fuel height and 0.20 m row spacing; (c) buoyancy-driven burn, 1.22 m fuel height and 0.20 m row spacing; and (d) wind-driven burn, 0.61 m fuel height and 0.20 m row spacing, wind speed 2.2 m/s.

Downloaded By: [Webb, B. W.] At: 18:23 5 October 2010

row spacing. No filtering has been done in the spectra, and the strong fluctuations are representative of the complex signal. Further, the noise floor is evident when the power spectrum magnitude levels off at high frequency.

It is interesting to note that the power spectrum for both radiation and convection heat flux exhibits magnitudes that exceed the noise floor at frequencies as high as 50–70 Hz, depending on experimental condition. This suggests that fuel particles are exposed to temporal fluctuations in radiative and convective heating which are much more rapid than has been previously documented in the literature. The low-frequency (<0.1 Hz) content of the radiation flux is uniformly stronger than that of the convective flux, consistent with the time-series plots presented previously in which radiation transfer was seen to be more steady in time. On the other hand, all cases show that convection exhibits greater power at higher frequencies, suggesting convection transfer is more strongly governed by turbulent fluctuations in such

flames. Radiation and convection transfer do not exhibit significant frequency content beyond 50–70 Hz in the buoyancy-driven experiments (Figures 10a–c). Interestingly, the spectral content for radiation and convection flux for all fuel row spacings and heights in the buoyancy-driven burn configurations are quite similar, perhaps suggesting that radiation and convection flux are driven by the same turbulent combustion mechanisms. However, the wind-driven experiment (Figure 10d) displays significant spectral content in radiation and convection heat flux to 100 and 200 Hz, respectively. This is perhaps the result of increased high-frequency turbulence induced by the forced flow. Although these data reveal that rather high frequencies do exist in these laboratory-scale fires, it is unknown just how fuel particles may react to fluctuations in heat flux at these frequencies. Clearly more study must be undertaken to understand the significance.

CONCLUSIONS

This study reports experimental measurements of time-resolved convective and radiative heat flux in discrete fuel beds designed to simulate natural fuels present in wildland fires. The influence of fuel row spacing and height on heat transfer characteristics were investigated for both buoyancy- and wind-driven flow. The results show the effect of discrete combustion characteristics of fuel rows on radiation pre-heating. Whereas radiation transfer is felt long before flame arrival, the convective heating occurs abruptly when the combustion occurs. Convective cooling is evident during intervals of radiative preheating prior to flame arrival, and during high-amplitude turbulent fluctuations after flame arrival. Turbulent temporal fluctuations in convective flux are more rapid than previously documented, with content at frequencies as high as 50–70 Hz for buoyancy-driven flames, and 150–200 Hz for wind-assisted flames. Temporal fluctuations in the radiative flux are confined more principally to low frequencies. Successively stronger convective heating pulses are exhibited immediately prior to ignition in nearly all cases, suggesting that convective energy transport may be critical to the flame jumping across discrete fuel gaps. The influence of ambient wind field seems to be primarily demonstrated through increased convective heating just before and after ignition. However, wind does not necessarily result in increased cumulative heat load. It appears that in both the buoyancy- and wind-driven experiments the energy levels significantly exceed that required to effect ignition. Finally, the flame spread rate data suggest that the advance of the combustion is primarily influenced by the strength of the convective flow, either buoyancy- or wind-driven.

ACKNOWLEDGMENTS

This work was supported in part by funding provided by the U.S. Forest Service and the National Fire Plan. The assistance of Anita Hershman and Danette Paige in preparing fuel beds is appreciated.

REFERENCES

Anderson, H.E. 1968. Flame shape and fire spread. *Fire Tech.*, (Feb.), 51–58.

Anderson, H.E. 1969. *Heat Transfer and Fire Spread*, Intermountain Forest and Range Experiment Station, Forest Service, U.S. Department of Agriculture, Ogden, UT.

Downloaded By: [Webb, B. W.] At: 18:23 5 October 2010

Babrauskas, V. 2003. *Ignition Handbook*, Fire Science Publishers, Issaquah, WA.

Butler, B.W. 1993. Experimental measurements of radiant heat fluxes from simulated wildfire flames. *Twelfth International Conference on Fire and Forest Meteorology*, Jekyll Island, Georgia, Society of American Foresters.

Butler, B.W., Cohen, J., Latham, D.J., Schuette, R.D., Sopko, P., Shannon, K.S., Jimenez, D., and Bradshaw, L.S. 2004. Measurements of radiant emissive power and temperatures in crown fires. *Can. J. For. Res.*, **34**, 1577–1587.

Catchpole, E.A., Catchpole, W.R., and Rothermel, R.C. 1993. Fire behavior experiments in mixed fuel complexes. *Int. J. Wildland Fire*, **3**, 45–57.

Catchpole, W.R., Catchpole, E.A., Butler, B.W., Rothermel, R.C., Morris, G.A., and Latham, D.J. 1998. Rate of spread of free-burning fires in woody fuels in a wind tunnel. *Combust. Sci. Technol.*, **131**, 1–37.

Churchill, S.W., and Bernstein, M. 1977. Correlating equation for forced convection from gases and liquids to a circular cylinder in crossflow. *ASME J. Heat Transfer*, **99**, 300–306.

De Mestre, J.J., Catchpole, E.A., Anderson, D.H., and Rothermel, R.C. 1989. Uniform propagation of a planar fire front without wind. *Comb. Sci. Technol.*, **65**, 231–244.

Dupuy, J.L. 2000. Testing two radiative physical models for fire spread through porous forest fuel beds. *Comb. Sci. Technol.*, **155**, 149–180.

Fons, W.L. 1946. Analysis of fire spread in light forest fuels. *J. Agriculture Res.*, **72**, 93–121.

Frankman, D.J. 2009. Radiation and convection heat transfer in wildland fire environments. PhD dissertation, Brigham Young University, Provo, UT.

Hottel, H.C., Williams, G.C., and Steward, F.R. 1965. The modeling of firespread through a fuel bed. *Tenth Symp. (Int.) Comb.*, The Combustion Institute, Pittsburgh, PA.

Jakob, M. 1949. *Heat Transfer*, Wiley, New York, Vol. 1.

Konev, E.V., and Sukhinin, A.I. 1977. The analysis of flame spread through forest fuel. *Combust. Flame*, **28**, 217–223.

Pagni, P.J. 1972. Flame spread through porous fuels. *Fourteenth Symp. (Int.) Comb.*, The Combustion Institute, Pittsburgh, PA.

Santoni, P.A., Balbi, J.H., and Dupuy, J.L. 1999. Dynamic modelling of upslope fire growth. *Int. J. Wildland Fire*, **9**, 285–292.

Telisin, H.P. 1973. Flame radiation as a mechanism of fire spread in forests. In Afgan, N.H. and Beer, J.M. (Eds.), *Heat Transfer in Flames*, Wiley, New York, Vol. 2, pp. 441–449.

Van Wagner, C.E. 1967. Calculations on forest fire spread by flame radiation. *Special paper for the 6th World Forestry Conference:* 1–14. See also Can. Dept. For. Rep. No. 1185, 28 pages.

Vatell Corporation. 2007. *HFM*. Retrieved 18 October 2007 from http://www.vatell.com/hfm.htm

Downloaded By: [Webb, B. W.] At: 18:23 5 October 2010